

Imaging the circumstellar envelopes of AGB stars *

N. Mauron¹ and P. J. Huggins²

¹ Groupe d'Astrophysique, UMR 5024 CNRS, Case CC72, Place Bataillon, F-34095 Montpellier Cedex 5, France e-mail: mauron@graal.univ-montp2.fr

² Physics Department, New York University, 4 Washington Place, New York NY 10003, USA

Received xxx/ Accepted xxx

ABSTRACT

Aims. We report the results of an exploratory program to image the extended circumstellar envelopes of asymptotic giant branch (AGB) stars in dust-scattered galactic light. The goal is to characterize the morphology of the envelopes as a probe of the mass-loss process.

Methods. The observations consist of short exposures with the VLT and longer exposures with 1–2 m telescopes, augmented with archival images from the Hubble Space Telescope.

Results. We observed 12 AGB stars and detected the circumstellar envelopes in 7. The detected envelopes have mass loss rates $\gtrsim 5 \times 10^{-6} M_{\odot} \text{ yr}^{-1}$, and they can be seen out to distances $\gtrsim 1 \text{ kpc}$. The observations provide information on the mass loss history on time scales up to $\sim 10,000 \text{ yr}$. For the five AGB envelopes in which the circumstellar geometry is well determined by scattered light observations, all except one (OH348.2–19.7) show deviations from spherical symmetry. Two (IRC+10216 and IRC+10011) show roughly spherical envelopes at large radii but asymmetry or bipolarity close to the star; one (AFGL 2514) shows an extended, elliptical envelope, and one (AFGL 3068) shows a spiral pattern. The non-spherical structures are all consistent with the effects of binary interactions.

Conclusions. Our observations are in accord with a scenario in which binary companions play a role in shaping planetary nebulae, and show that the circumstellar gas is already partly shaped on the AGB, before evolution to the proto-planetary nebula phase.

Key words. Stars: AGB and post-AGB – Stars: mass loss – Stars: circumstellar matter

1. Introduction

One of the most striking aspects of the evolution of stars from the asymptotic giant branch (AGB) to the planetary nebulae (PN) phase is the complex structure formed in the circumstellar gas (e.g., Balick & Frank 2002). This has been extensively observed in PNe using high resolution optical imaging with the Hubble Space Telescope (HST), and shows both large and small scale features such as multiple arcs, bubbles, bicones, point-symmetric knots and bullets, tori, ansae, and globules. Many examples can be seen in the recent volume edited by Meixner et al. (2004).

Some of the structural features in the nebulae are related to photo-ionization or fast winds produced during the PN phase, but others are formed earlier and are only partly understood. The multiple arcs are known to result from modulation of the mass-loss during the late AGB

phase (Mauron & Huggins 2000), although the underlying mechanism is unknown. Similarly, the point symmetries seen in PNe can be traced to the effects of bipolar jets which become prominent in the proto-PN phase (e.g., Lopez 2003), but the detailed picture is not clear. The uncertain, early development of these jets and their possible links to other structural features such as disks or tori which emerge from the last major episodes of mass-loss underscore the importance of observations of the final stages of the AGB.

The detailed structure of the circumstellar envelopes of AGB stars has not been studied in a large number of cases because the relatively cool material is a challenge to high resolution observations. One technique that has been used to image the circumstellar gas is millimeter interferometry, and the most extensive work in this area is by Neri et al. (1998) who produced an atlas of AGB envelopes in the molecular lines of CO. With an angular resolution of $\sim 3'' \times 5''$ and limited dynamic range, they conclude that most (70%) AGB envelopes are consistent with spherical symmetry. A second technique that has been used to ob-

Send offprint requests to: N. Mauron

* Based on observations made at the European Southern Observatory, Chile (program 63.I-0177A), on de-archived data made with the NASA/ESA *Hubble Space Telescope*, and on observations made at Haute-Provence Observatory, France

Table 1. The observed sample of AGB stars

Star	IRAS name	<i>l</i>	<i>b</i>	C/O	<i>d</i> (pc)	<i>V</i> _{exp} (km s ⁻¹)	\dot{M} (M _{sun} yr ⁻¹)	<i>f</i> ₁₂ (Jy)	<i>f</i> ₁₂ / <i>f</i> ₂₅	Note
IRC+10011	01037+1219	128	-50	O	740	20.7	2.2 10 ⁻⁵	1155	1.19	(1)
YY Tri	02152+2822	145	-31	C	2100	9.2	0.2 10 ⁻⁵	121	1.08	
IK Tau	03507+1115	178	-31	O	300	19.6	0.5 10 ⁻⁵	4634	1.95	(1)
IRC+70066	05411+6957	143	+20	O	730	21.9	0.4 10 ⁻⁵	801	1.97	(1)
AFGL 5254	09116-2439	253	+16	C	1170	13.1	1.4 10 ⁻⁵	737	1.85	(1)
CIT 6	10131+4039	198	+56	C	460	16.8	0.8 10 ⁻⁵	3319	2.72	(1)
AFGL 2155	18240+2326	52	+15	C	1070	16.1	1.6 10 ⁻⁵	731	1.63	(1)
OH 348.2-19.7	18467-4802	348	-19	O	1200	12.3	0.8 10 ⁻⁵	284	0.83	
AFGL 2514	20077-0625	36	-20	O	660	16.2	0.8 10 ⁻⁵	1255	1.18	
AFGL 3068	23166+1655	93	-40	C	1080	14.1	4.2 10 ⁻⁵	706	0.91	(1)
AFGL 3099	23257+1038	92	-47	C	1300	10.1	0.5 10 ⁻⁵	190	1.34	
AFGL 3116	23320+4316	108	-17	C	870	14.7	1.1 10 ⁻⁵	959	2.04	(1)

Notes: (1) *d* and \dot{M} from Olivier et al. (2001), otherwise from Loup et al. (1993)

serve the envelopes is imaging the thermal infrared dust emission. This is possible at very high angular resolution, and studies of individual objects have revealed asymmetries very close to the central stars (e.g., Monnier et al. 2004, Weigelt et al. 2002).

A third technique of imaging the circumstellar dust in scattered light at optical wavelengths has been used by us in the case of the nearby AGB archetype IRC+10216 (Mauron & Huggins 1999, 2000). The inner envelope is illuminated by light from the central star, and the outer envelope is illuminated by the ambient galactic radiation field. With ground based and HST observations, the observations provide a resolution of 0''.1-1'' over a very large field, and in the case of IRC+10216, we were able to detect scattered light out to 200'' from the central star and to determine the detailed geometry of the envelope.

In this paper we report on a pilot survey to explore the extent to which this technique can be used to study the large scale structure of the circumstellar envelopes of much more distant AGB stars.

2. The AGB sample

The AGB stars observed in the survey are listed in Table 1. They were selected from the catalog of Loup et al. (1993) with priority given to nearby objects with strong IRAS fluxes and large infrared excesses. They were also chosen to lie at relatively high galactic latitudes, in order to minimize galactic extinction and to avoid crowded background star fields. The sample contains 12 objects. It is not complete with regard to any observable quantity, but should be regarded as an exploratory sample, going beyond the single case of IRC+10216 reported earlier.

Table 1 lists for each object the IRAS name, the galactic co-ordinates, the chemistry (oxygen-rich or carbon-rich), distance *d*, expansion velocity *V*_{exp}, mass-loss rate \dot{M} , and relevant IRAS fluxes from the point source catalog. If available, the values of *d* and \dot{M} are taken from

Olivier et al. (2001) in which distances were determined through the period luminosity relation, otherwise they are from Loup et al. (1993).

3. Observations

Details of the observations including the telescopes, the filters, and the exposure times are listed in Table 2.

IRC+10011, OH 348.2-19.7, and AFGL 5254 were observed with the ESO VLT using the FORS1 focal reducer. Relatively short exposures were made in U, B, & V filters. The images are 6''.8 \times 6''.8 with a pixel size of 0''.200, and the image quality is generally near 1''.1 (FWHM).

AFGL 2155, AFGL 3068, AFGL 3099, AFGL 3116, YY Tri, IK Tau, IRC+70066 and CIT6 were observed with the 1.20 m telescope of the Observatoire de Haute-Provence (OHP). This telescope is equipped with a camera which provides a field of 11''.7 \times 11''.7 with a pixel size of 0''.684. In cases where the object was not easily identified, the observations were started with a short I band exposure which typically results in a clear identification, followed by longer exposures in B and V. In a few cases U band exposures were also obtained. The image quality is \sim 2-3'' (FWHM).

AFGL 2514 was observed with the ESO Danish 1.54 m telescope using the DFOSC focal reducer, and only in the V band. The image size is 13''.7 \times 13''.7 with a pixel size 0''.403. The image quality is 1''.0.

All CCD frames were reduced using standard procedures including bias subtraction, flat-field correction, and cosmic-ray rejection. When several frames were made with the same passband, the frames were appropriately shifted and summed.

Where available we also made use of images from the HST archives to complement our observations at high resolution. Relevant data was found in four cases, and details are given in Table 3. These data consist of ACS images, with a field size of 211'' \times 211'' and scale 0''.050 per pixel.

Table 3. Details of the HST Archival Observations

Star	Dataset	Filter	Exposure (min)
IRC+10011	j8di89dmq	F814W	11.3
	j8di89drq		
OH 348.2–19.7	j92k41doq	F606W	11.6
	j92k41dtq		
AFGL 2514	j92k52i4q	F606W	11.6
	j92k52i9q		
AFGL 3068	j92k58h0q	F606W	23.1
	j92k58h1q		
	j92k58h2q		
	j92k58h3q		

Data reduction included co-addition of the images, correction for cosmic ray hits, and rotation for direct comparison with the ground based images. As far as we are aware, none of these HST data have previously been published.

4. The circumstellar envelopes

4.1. The images

The circumstellar envelopes were detected in scattered light around 7 of the AGB stars observed, and not detected around 5. Images and intensity profiles are discussed individually in §4.3.

The images shows that the envelopes can be illuminated as in IRC+10216 in two ways, by the central star or by the ambient galactic radiation field. In the first case, the central star forms a small scattering core whose intensity decreases rapidly with angular distance from the center ($\sim \theta^{-3}$, Martin & Rogers 1987). In the second case, a faint, extended nebula is seen, with a relatively shallow radial dependence (see below), and it may form a plateau in the central regions where the optical depth to external radiation exceeds ~ 1 . Both effects may occur at the same time. The typical situation in the thicker envelopes is that the star and the star-illuminated core are faint or not seen in the B or V bands, but the star becomes dominant at longer wavelengths because of its low temperature and the decreasing opacity of the dust envelope.

4.2. Surface brightness

For each circumstellar envelope we determined the V-band surface brightness, either at the center if no core was visible, or at an offset away from the center if the core was seen. The results are given in column 5 of Table 2. Upper limits are given for the cases where the extended envelope was not detected. For comparison, the V-band surface brightness of the central plateau of IRC+10216 is $25.2 \text{ mag arcsec}^{-2}$ (Mauron et al. 2003).

Where possible, the surface brightness of the envelopes was calibrated by using counts of photometric standard

stars imaged on the same night. Where this was not possible, the image calibration was based on photometric data for field stars from the APM catalog (Irwin 2000). By considering the blue and red APM photometry for several sequences with Johnson UBV photometry, it was possible to derive the following relations between Johnson and APM magnitudes:

$$V \approx 0.5 * (B_{APM} + R_{APM}) - 0.4, \text{ and}$$

$$B \approx B_{APM} - 0.2.$$

with a scatter for these relations of ~ 0.2 mag. There is good consistency in cases where both methods can be applied to the same envelope, but because the envelopes are faint, i.e., a few percent of the sky brightness, the quality of the surface brightness measurements is also affected by sky noise, and the final error bars are estimated to be around ± 0.4 mag. In the case of IK Tau, CIT 6, and AFGL 3116, the V-band brightness was estimated from the B-band image, using the assumption that $B-V=0.5$, which is the color measured for IRC+10216 (Mauron et al. 2003).

4.3. Individual envelopes

4.3.1. IRC+10011 (WX Psc, CIT 3)

The V-band image of IRC+10011 obtained with the VLT is shown in the left hand panel of Fig. 1. It shows a bright core illuminated by the central star, and a faint, extended envelope illuminated by the ambient radiation field. The U and B-band images are similar, although the central core is suppressed at the shorter wavelengths.

The images of the extended envelope appear approximately circularly symmetric, and this is seen more clearly in the close-up isophotal plot of the V-band image in Fig. 2 (left). Intensity strips in azimuth, averaged in sectors of 20° show variations of less than 15%. The radial variation of the envelope in B and V (averaged in azimuth) is shown in Fig. 2 (right). The envelope can be traced out to $\sim 50''$; the limitation is set by variations in the background level.

The HST-ACS image of IRC+10011 in the far red F818W filter is shown in the right hand panel of Fig. 1. In this image the star is dominant, and only the innermost regions of the envelope are seen. To the NW at $\sim 0''.8$ from the center there is part of a faint circular arc, probably similar to the arcs seen in IRC+10216. However, in contrast to the outer envelope, the core structure is highly asymmetric, with a bright extension out to $\sim 0''.4$ at $PA \sim -45^\circ$.

The inner envelope of IRC+10011 has also been studied at high resolution by Hofmann et al. (2001) using bispectrum speckle interferometry in the J, H, and K bands. The core is found to be point-like in H and K, but in J it is elongated along a symmetry axis at $PA \sim -28^\circ$ out to distances of ~ 200 mas. It seems most likely that the HST image captures the extension of this core asymmetry. Thus IRC+10011 is somewhat similar to the case

Table 2. Details of the Observations

Star	Telescope	Band & Exposure (min)	V/B Image ^a	Surface Brightness (V-mag arcsec ⁻²)	Notes
IRC+10011	VLT 8.00 m	U (4), B (2), V (2)	st + env	25.7 (at 5'')	1
YY Tri	OHP 1.20 m	B (240), V (120)	< 25.1	
IK Tau	OHP 1.20 m	U (90), B(150)	st	< 24.9 (at 10'')	2
IRC+70066	OHP 1.20 m	U (480), B (420), V (330)	st	< 25.8 (at 10'')	
AFGL 5254	VLT 8.00 m	U (4), B (2), V (2)	st	< 25.4 (at 5'')	
CIT 6	OHP 1.20 m	U (102), B (120)	st	< 24.9 (at 10'')	2
AFGL 2155	OHP 1.20 m	V (300)	env	25.3	
OH 348.2–19.7	VLT 8.00 m	U (8), B (2), V (2)	env	24.9 (at 5'')	1, 3
AFGL 2514	ESO 1.54 m	V (120)	env	23.6	1
AFGL 3068	OHP 1.20 m	B (60), V (60)	env	23.9	1
AFGL 3099	OHP 1.20 m	V (240)	env	26.0	
AFGL 3116	OHP 1.20 m	B (150), V (60)	st + env	25.8	2, 4

^a Detections in the V and B images: st = star, env = envelope. The star YY Tri is seen only in the I-band.

Notes: (1) See Table 3 for HST data. (2) Surface brightness from B image, assuming B–V = 0.5. (3) Star near center is field star. (4) Envelope seen only in B image.

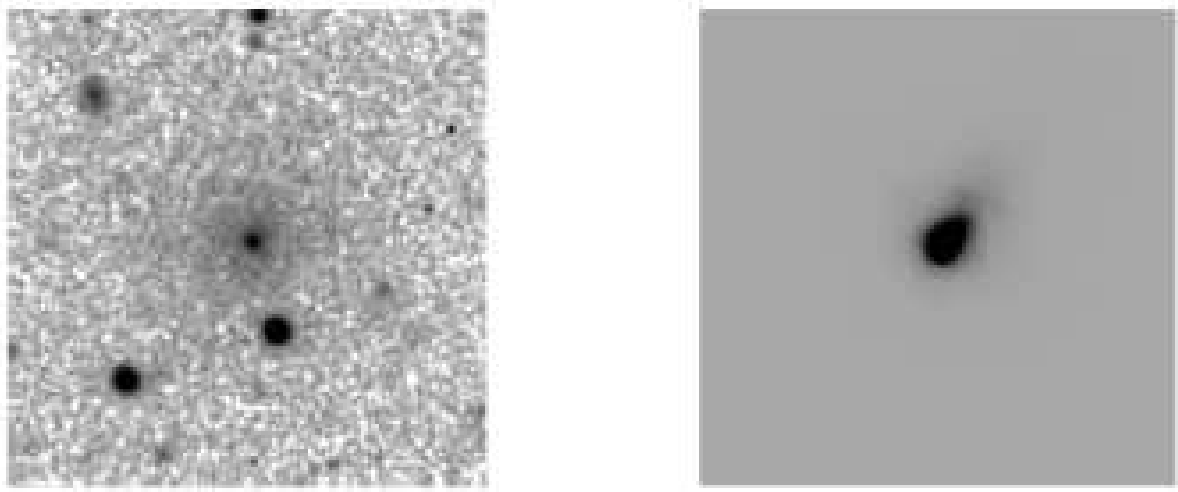


Fig. 1. IRC+10011. *Left:* VLT image in the V-band. Field size: 51''.2 × 51''.2. *Right:* HST-ACS image in the F816W filter. Field size: 6''.4 × 6''.4. North is up and east is to the left in all images.

of IRC+10216 where approximate circular symmetry and shells in the extended envelope co-exist with a strong axial symmetry close to the star.

4.3.2. OH 348.2–19.7

The V-band image of OH 348.2–19.7 obtained with the VLT is shown in the left hand panel of Fig. 3. The B-band image is similar. The extended envelope is clearly detected in both images and at first sight looks unusual because it

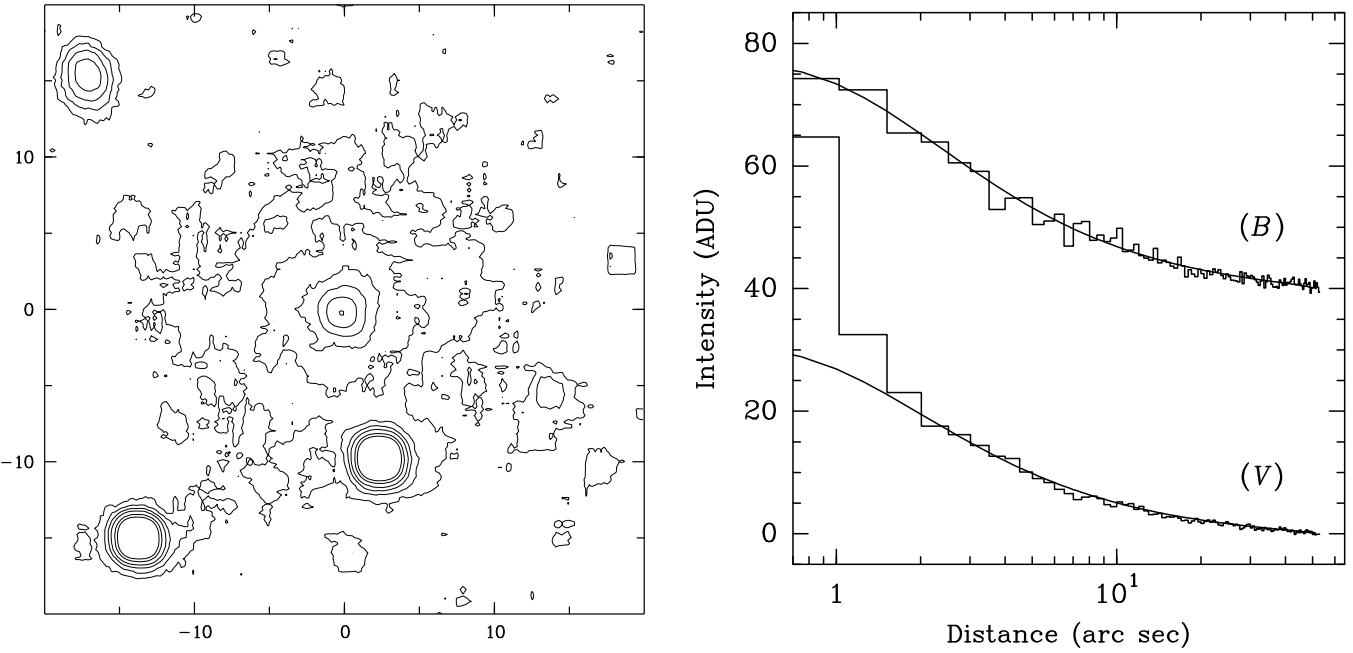


Fig. 2. IRC+10011. *Left:* Close-up isophotes of the VLT V-band image. Field size: $40'' \times 40''$. *Right:* Radial profiles, averaged in azimuth, from the VLT images in B and V. In the V profile, 1 ADU above the background corresponds to 2.0×10^{-16} $\text{erg s}^{-1} \text{cm}^{-2} \mu\text{-}1 \text{arcsec}^{-2}$, or 28.2 V-mag arcsec^{-2} . No calibration was possible for the B profile. The B data are scaled by a factor of 4.2 and offset from zero for clarity. The solid lines show model fits to the profiles for a constant mass loss rate. See text for details.

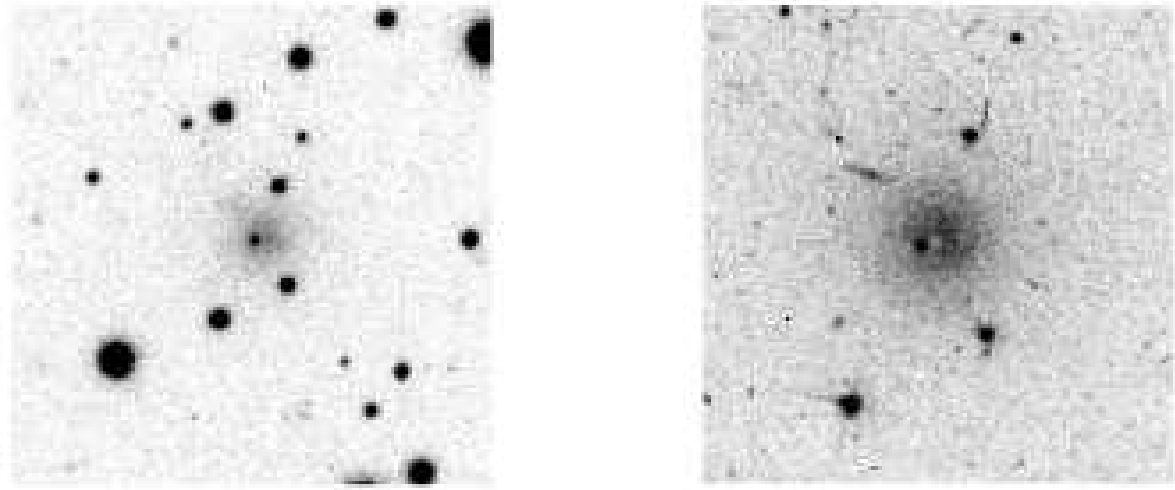


Fig. 3. OH 348.2-19.7. *Left:* VLT image in the V-band. Field size: $51''2 \times 51''2$. *Right:* HST-ACS image in the F606W filter. Field size: $25''6 \times 25''6$.

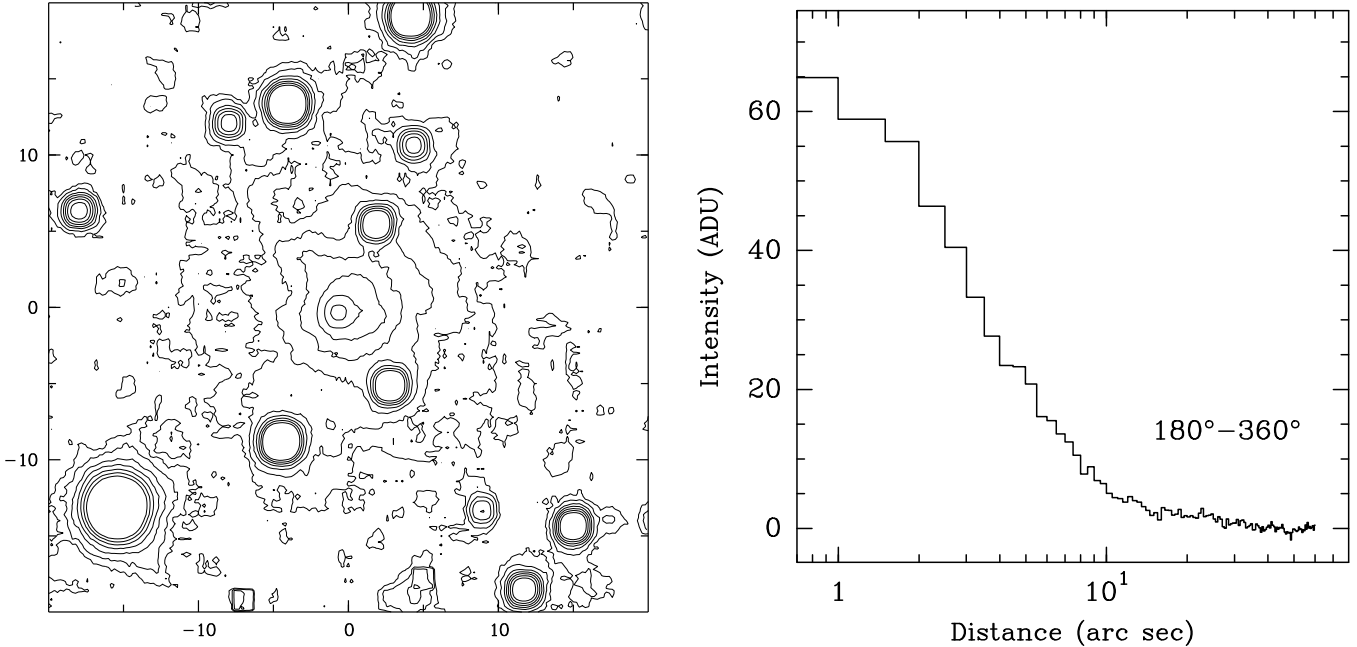


Fig. 4. OH 348.2–19.7. *Left:* Close-up isophotes of the VLT V-band image. Field size: $40'' \times 40''$. *Right:* Radial intensity profile from the V-band image. In this profile, 1 ADU above the background corresponds to $2.0 \times 10^{-16} \text{ erg s}^{-1} \text{ cm}^{-2} \mu^{-1} \text{ arcsec}^{-2}$, or $28.2 \text{ V-mag arcsec}^{-2}$.

is not centered on the star within the nebula, and there is an extension to the north-east.

The HST-ACS red (F606W) image is shown in the right hand panel of Fig. 3. It too shows a star offset from the center of the nebula, but reveals that the extension to the north-east in the VLT image is a background galaxy. The issue of the star is resolved at longer wavelengths where 2MASS images and a far red (F814W) HST image show that the true central star is not seen in Fig. 3. It lies $\sim 0''.65$ to the west of the visible star, which is a foreground or background object. This conclusion is supported by the absence of core brightening in the nebula around the visible star.

When allowance is made for these features of the VLT images of OH 348.2–19.7, the overall appearance of the extended envelope is approximately circular, as seen in the close-up isophotal image in Fig. 4 (left). To the west where the field is clearest, the envelope can be traced out to distances of $28''$ (Fig. 4, right). The HST image shows that approximate circular symmetry continues into the inner regions. It shows a dip in the intensity at the center, which is expected for an optically thick, externally illuminated envelope, as is seen in the case of IRC+10216 (Mauron & Huggins 1999). There is also a slight east-west asymmetry in the brightness which suggests a slightly asymmetric illumination.

4.3.3. AFGL 2514

The V-band image of AFGL 2514 obtained with the ESO 1.54 m telescope is shown in the left hand panel of Fig. 5. This is the brightest envelope detected in the survey

(Table 2), even though it is not exceptional with regard to color or mass loss rate relative to the other objects. No central core is seen, but the envelope is detected with a good signal-to-noise ratio.

The envelope shows a remarkably non-spherical morphology, which is seen more clearly in the close-up isophotal image in Fig. 6 (left). The contours are approximately elliptical, with the ratio of the major to minor axis of ~ 1.4 . There is no evidence to suggest that the shape is due to asymmetric illumination. Radial intensity strips (Fig. 6, right) show that the envelope can be detected out to $\sim 40''$.

The HST image of AFGL 2514 in the red F606W filter is shown in the right hand panel of Fig. 5. It is affected by pattern noise, but is of sufficient quality to confirm the elliptical shape of the envelope. This image shows a point-like object at the center of the nebula, and a further HST image in the far red F814W filter shows it to be brighter and slightly extended. This is confirmed to be the AGB star by comparison with 2MASS images.

4.3.4. AFGL 3068

The V-band image of AFGL 3068 obtained with the OHP 1.20 m telescope is shown in Fig. 7 (left). The B-band image is similar. Neither shows the central star, but the envelope is well detected in both images. The scattered light can be detected out to a distance of $\sim 40''$ from the center, and the distribution is asymmetric. Although the diffraction spike of the bright star in the field covers part of the scattered light image, the envelope is seen to be convex to the north-west at $PA \sim -30^\circ$, suggesting that a

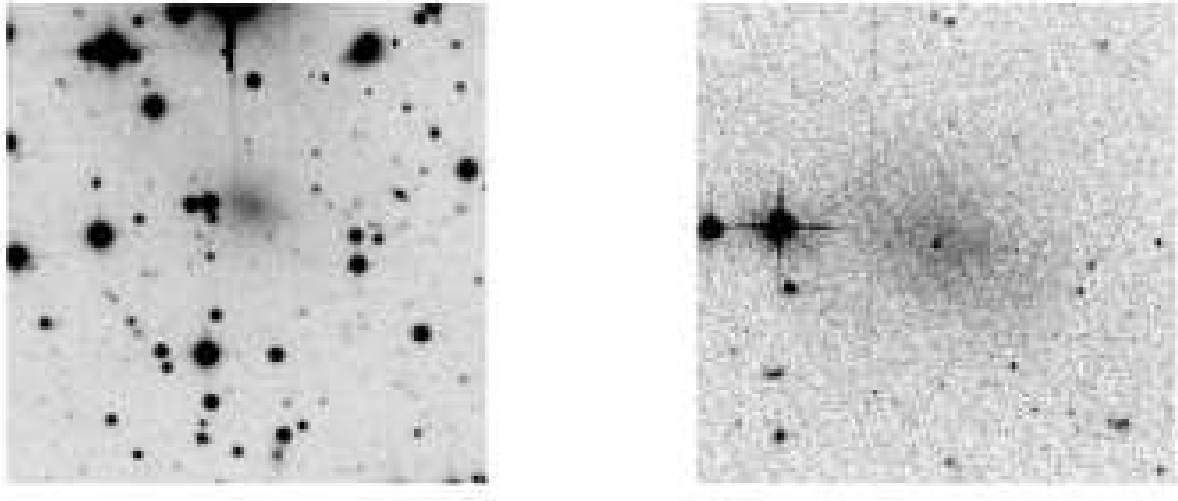


Fig. 5. AFGL 2514. *Left:* ESO 1.54 m image in the V-band. Field size: $102'' \times 102''$. *Right:* HST-ACS image in the F606W filter. Field size: $25.''6 \times 25.''6$.

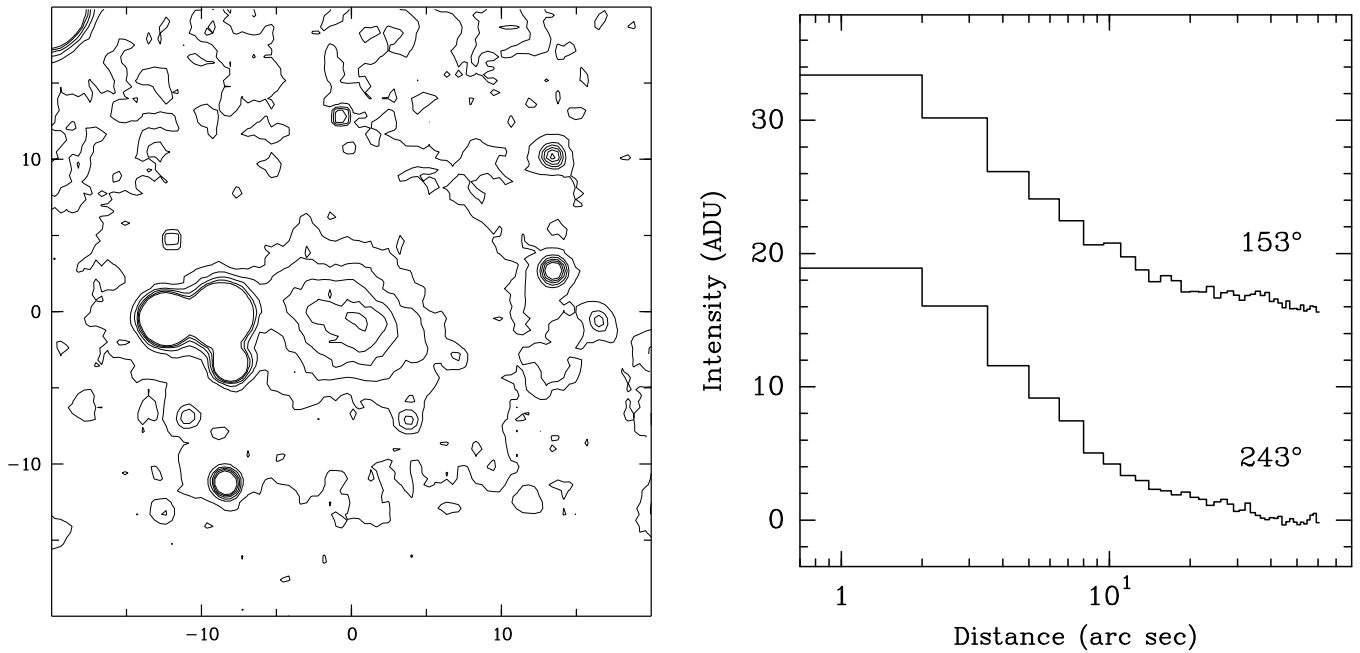


Fig. 6. AFGL 2514. *Left:* Close-up isophotes of the ESO 1.54 m V-band image. Field size: $40'' \times 40''$. *Right:* Radial profiles in the V-band along the major and minor axes. The intensities are scaled down by 100, and the upper profile is offset for clarity. The top of both profiles corresponds to $1.4 \times 10^{-14} \text{ erg s}^{-1} \text{ cm}^{-2} \mu\text{-band}^{-1} \text{ arcsec}^{-2}$, or $23.6 \text{ mag-V arcsec}^{-2}$.

component of the external illumination comes from this direction.

The HST image of AFGL 3068 in the red F606W filter (Fig. 7, right) confirms the directed external illumination, and in addition reveals a remarkable spiral pattern in the

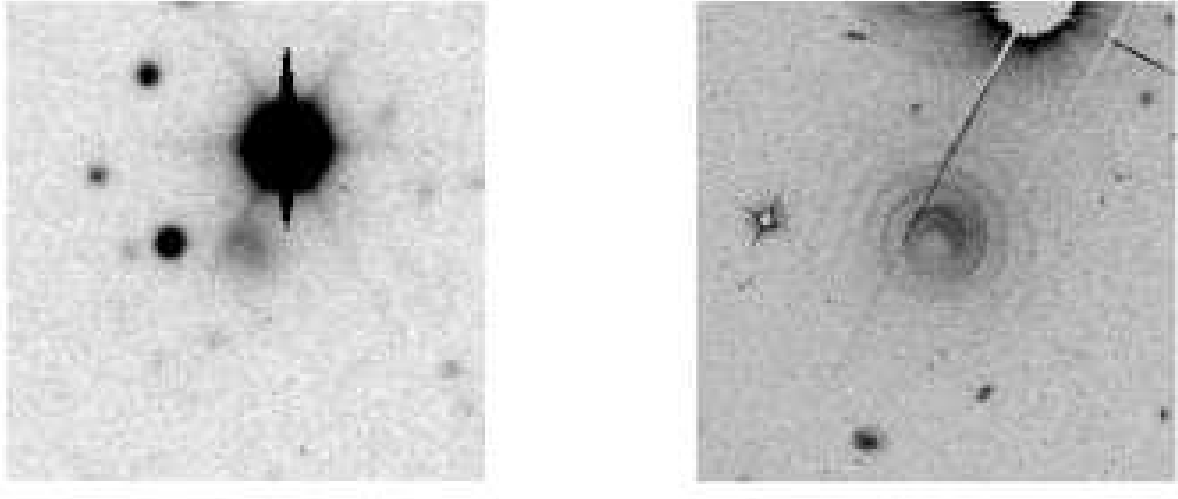


Fig. 7. AFGL 3068. *Left:* OHP 1.20 m image in the V-band. Field size: $117'' \times 117''$. *Right:* HST-ACS image in the F606W filter. Field size: $51''2 \times 51''2$.

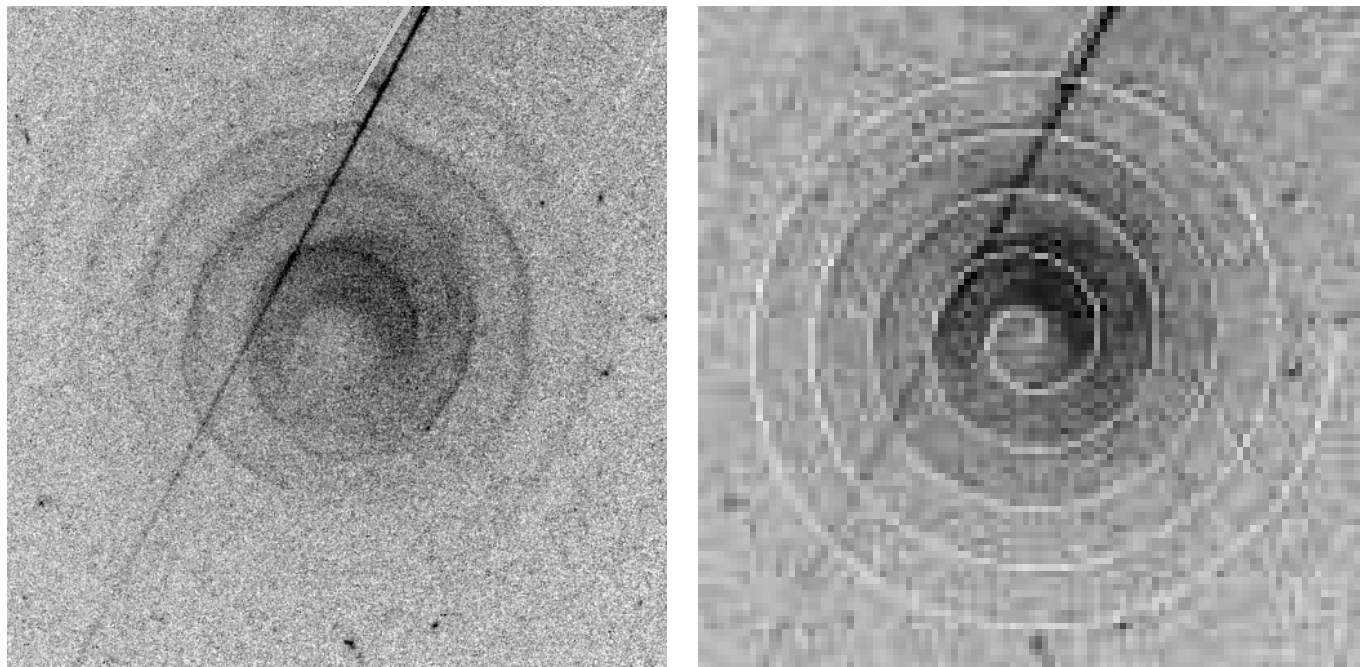


Fig. 8. AFGL 3068. *Left:* Close-up of HST-ACS image in the F606W filter. Field size: $25''6 \times 25''6$. *Right:* Same image, with Archimedes spiral fit. See text for details. *This Fig. is available in color in the on-line version of the paper*

envelope (see also Appendix A). No central star is seen, but this becomes visible at longer wavelengths in 2MASS

images and in an HST far red F814W image. The star lies at the center of the pattern.

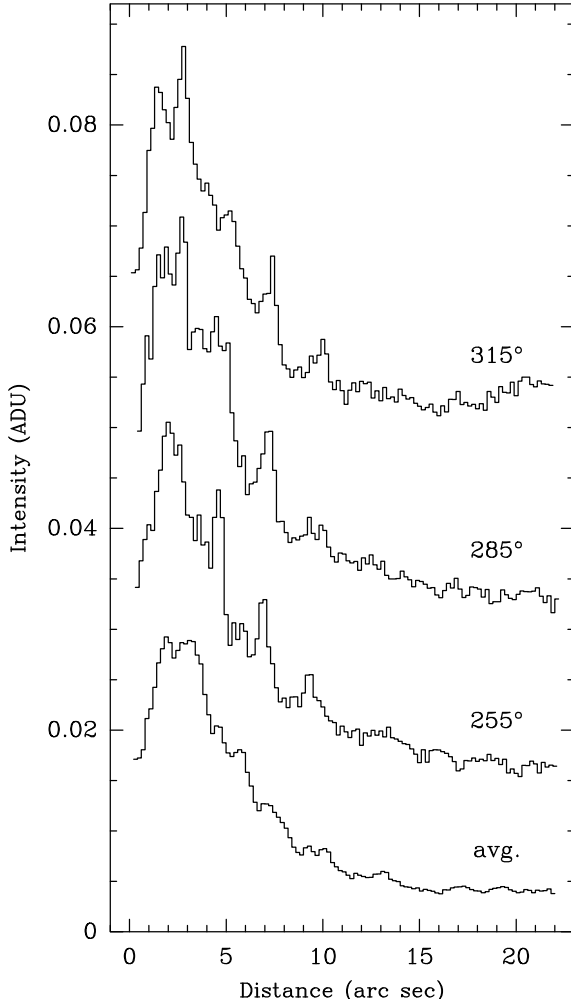


Fig. 9. AFGL 3068. Radial profiles in the F606W filter. The top three profiles are for adjacent 30° sectors and are labeled with the position angle. The maximum of the bottom curve corresponds to $1.1 \times 10^{-14} \text{ erg s}^{-1} \text{ cm}^{-2} \mu^{-1} \text{ arcsec}^{-2}$, or $23.9 \text{ V-mag arcsec}^{-2}$.

The spiral pattern is single-armed, and can be traced out to a distance of $12''$ from the center (Fig. 8; *this Fig. is available in color in the on-line version of the paper*). Radial intensity profiles in consecutive azimuthal sectors are shown in Fig. 9. The widths of the spiral feature are partly resolved and the peak intensities exceed the adjacent lines of sight by factors of up to ~ 2.5 . It can be seen in Fig. 9 that the radial profiles of the spiral are typically steep on the side away from the star and less steep on the side toward the star, which is characteristic of thin shells, as described by Mauron & Huggins (2000). Using a simple model of nested shells to interpret the profiles, we find that the widths are $\lesssim 0''.5$ and the amplitudes correspond to density contrasts between the arm and the inter-arm material of factors up to ~ 5 .

The pattern itself closely resembles a true Archimedes spiral, in which the inter-arm spacing is constant. The equation for this is $\theta = A\phi + C$, where θ is the angular distance from the center, ϕ is the azimuthal angle (measured counter clockwise from the west), and A and C are

constants which determine the inter-arm separation and the orientation on the sky, respectively. A least squares fit to the pattern gives:

$$\theta = 0.364(\pm 0.001)\phi + 0.38(\pm 0.01)$$

where θ is in arcseconds, and ϕ is in radians. The fit is shown superposed on the image in Fig. 8 (right), where the origin of the spiral corresponds to the location of the central star. The generation of the spiral is discussed in §5.3.

4.3.5. AFGL 2155, AFGL 3099, and AFGL 3116

AFGL 2155, AFGL 3099, and AFGL 3116 are three carbon-rich AGB stars which were observed only with the OHP 1.20 m telescope. They were first observed in the I-band which showed bright point-like cores allowing identification by comparison with digitized red POSS images. Exposures in B and/or V were then made in order to image the envelope.

AFGL 2155 (Fig. 10) shows a bright envelope which is well detected in the V band image. It shows no stellar core, and the envelope can be traced out to a radial distance of $\sim 18''$ from the center. However, on account of its low galactic latitude, it lies in a relatively crowded star field and a foreground or background star near the center masks the large scale geometry of the envelope at low intensity levels.

AFGL 3099 (Fig. 11) and AFGL 3116 (Fig. 12) are the faintest envelopes detected in the survey. They lie in relatively open star fields and in azimuthally averaged radial profiles they can both be detected out to $\sim 20''$ from the center. The isophotal contours suggest that they may have interesting structure, but the signal-to-noise is too low to make any firm statement on the geometry.

5. Discussion

5.1. Envelope detection

The stars for which extended envelopes are detected in scattered light are generally those with the higher mass loss rates. The average mass loss rates for the detections and non-detections are 1.6 ± 0.5 and $0.7 \pm 0.2 \times 10^{-5} M_\odot \text{ yr}^{-1}$, respectively, with only a few overlapping cases. The dependence on mass loss rate is to be expected on the basis of the following considerations.

For envelopes with relatively high mass loss rates in which the stellar core is not seen, the intensity of the scattered light profile increases toward the center, but reaches a plateau level at a radial offset where the line of sight optical depth through the envelope reaches ~ 1 . Within the plateau, the intensity is roughly constant, or it may dip at the center if the optical depth is large. The width (FWHM) of the profile can be estimated by scaling the well-studied case of IRC+10216 (Mauron & Huggins

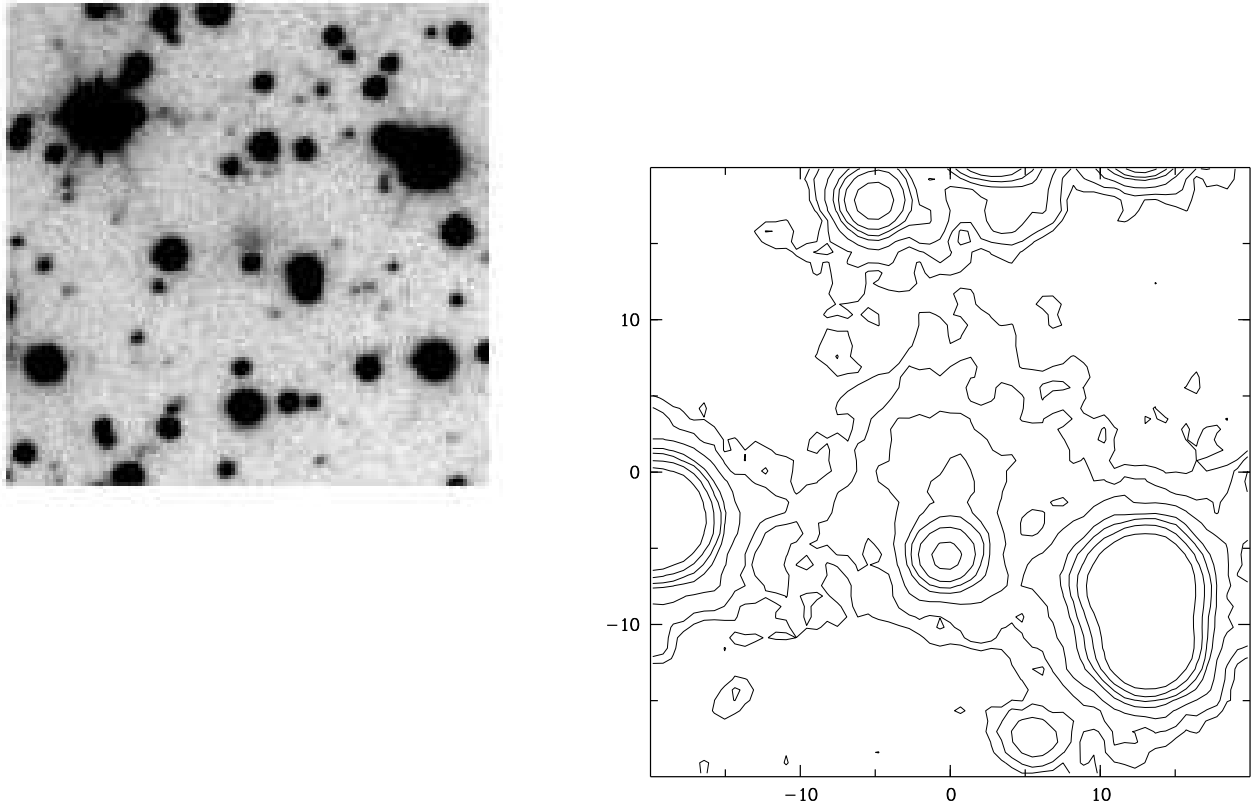


Fig. 10. AFGL 2155. *Left*: OHP 1.20 m image in the V-band. Field size is $117'' \times 117''$. *Right*: Close-up isophotes of the V-band image. Field size is $40'' \times 40''$.

2000), assuming similar grain properties and dust-to-gas ratios:

$$\Delta\theta = 5'' \left(\frac{\dot{M}}{10^{-5} M_{\odot} \text{ yr}^{-1}} \right) \left(\frac{V}{10 \text{ km s}^{-1}} \right)^{-1} \left(\frac{d}{1000 \text{ pc}} \right)^{-1}.$$

The effect of increasing distance is to reduce the angular size of the scattered light profile, but the surface brightness of the plateau level is independent of distance for a uniform galactic radiation field (ignoring interstellar extinction). If this level is above the threshold and the core region is resolved or partly resolved, the envelopes can be detected out to quite large distances $\gtrsim 1$ kpc.

For the envelopes detected here, the widths given by the above equation (2–14'') are roughly comparable to the widths measured in the profiles (4–12''), although there is no clear, overall correlation, suggesting that individual variations dominate the small dynamic range of the sample. Similarly, there is a variation in the peak brightness by a factor of ~ 10 . Besides intrinsic variation among the envelopes (e.g., their internal structure, or scattering properties), variation of the ambient galactic radiation field will also affect the visibility.

In the case of AFGL 3068, the morphology gives clear evidence that part of the illumination is contributed from a preferred direction. The source could well be the bright star seen in Fig. 7. From APM photometry, the magnitude of this star in V is about +12.0. If it is located at the same

distance from us as AFGL 3068 (see Appendix A), the angular separation of $28''$ between the two objects implies a physical separation of 0.15 pc. At this distance, the V-band illumination of the nebula by the bright star would be a factor of ~ 2 larger than the average interstellar radiation field. No other stars around AFGL 3068 appear to be good candidates for the source of the additional illumination.

There are five objects whose envelopes were not detected in scattered light. For one of these, YY Tri, the star is not seen in the B or V-bands. It probably has a thick envelope, but its large distance yields an estimated width of $\sim 0''.5$, which would make it undetectable with the current observations. In the other four cases, the estimated widths are somewhat larger (1–5''), but in each the central star is very bright (16–18 magnitudes) relative the surface brightness of scattered galactic light (e.g., $25.2 \text{ mag arcsec}^{-2}$ for IRC+10216). In these cases, the starlight scattered by the envelope (see equation 1 of Mauron & Le Borgne 1986), which has a steep radial dependence, is lost in the extended stellar profile of the ground-based observations. The limits on the galactic contribution (at offsets of 5'' or 10'') are therefore not very sensitive compared to the cases where the starlight is suppressed by a thick circumstellar envelope.

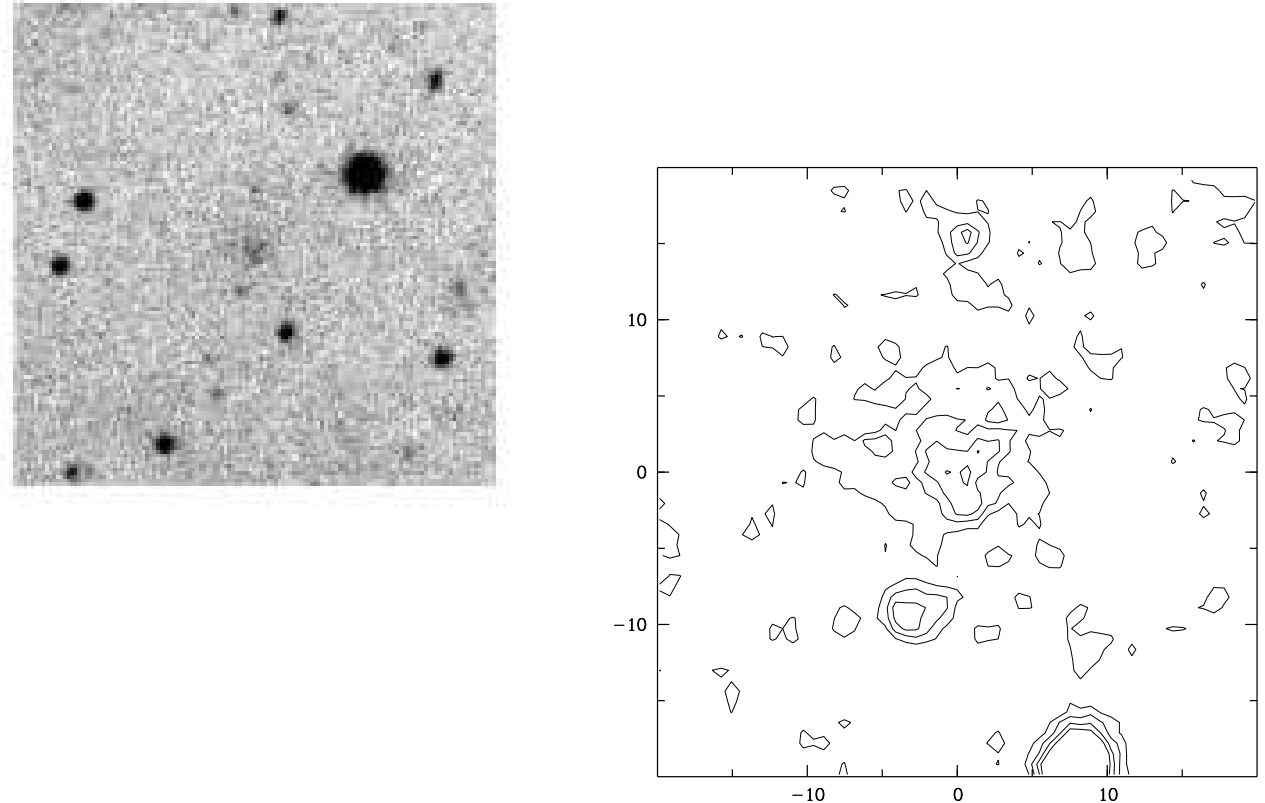


Fig. 11. AFGL 3099. *Left:* OHP 1.2 m image in the V-band. Field size: $117'' \times 117''$. *Right:* Close-up isophotes of the V-band image. Field size: $40'' \times 40''$.

5.2. Envelope time scales

Table 4 summarizes our observations of the envelopes in terms of their morphology, radial extent (θ_{env}), and the corresponding expansion time scale ($\tau_{\text{env}} = d\theta_{\text{env}}/V_{\text{exp}}$), using the distances and expansion velocities given in Table 1. We also give the morphology of the core (and the corresponding time scale) in cases where this differs from the extended envelope.

Table 4 includes data on the envelope of IRC+10216 which was observed by us in scattered light using ground-based and HST observations (Mauron & Huggins 1999, 2000). The extended envelope is detected out to a distance of $\sim 200''$, similar to that seen in CO (Huggins et al. 1988), and is roughly circular. In the central regions the envelope is bipolar. The WFPC2 F606W image shows a classic two-lobed structure, separated by a dark lane. We characterize the radial extent of the bipolar core by the radial distance to the outer 10% contour of each lobe ($1''.2$). Fainter light can be traced out to $\sim 6''$. Similar dimensions are found with the F814W filter (Skinner et al. 1998).

Table 4 also includes data on CIT 6. The extended envelope was not detected in the ground-based observations reported in Table 2. However, the stellar core was detected in HST WFPC2 images reported by Trammell (1999), Monnier et al. (2000), and Schmidt et al. (2002). The wide-V (F555W) image shows a classic two-lobed structure, like that in IRC+10216, and we characterize

the radial extent by the distance to the outer 10% contour of each lobe ($0''.3$); fainter light is seen out to beyond $1''$. The dimensions and appearance of the F675W image are similar. The larger scale structure of CIT 6 is not clear. At $\sim 10''$, millimeter CN observations show asymmetry, with a major/minor axis ratio of 1.4 oriented at a position angle -25° (Lindqvist et al. 2000), but at larger distances ($\sim 25''$) the envelope seen in CO appears circular (Neri et al. 1998). In scattered light at 1μ , Schmidt et al. (2002) identify arcs between $1''$ – $4''$ which may be similar to those seen in IRC+10216.

The observations summarized in Table 4 show that scattered light imaging can provide information about the mass loss on both short and relatively long time scales, up to $\sim 15,000$ yr. A detailed analysis of the time dependent rate of the mass loss is beyond the scope of the present report, but we illustrate the constraints provided by the observations for the case of IRC+10011 where, except for the core region, the envelope appears spherically symmetric.

In the right hand panel of Fig. 2 we compare the observed profiles of IRC+10011 with the results of a simple, analytical model for the scattered light. The model assumes uniform external illumination of an envelope with conservative scattering and an arbitrary phase function. Under these conditions the scattered light profile is given by: $I_s = I_o(1 - e^{-\tau})$, where I_o is the incident intensity and

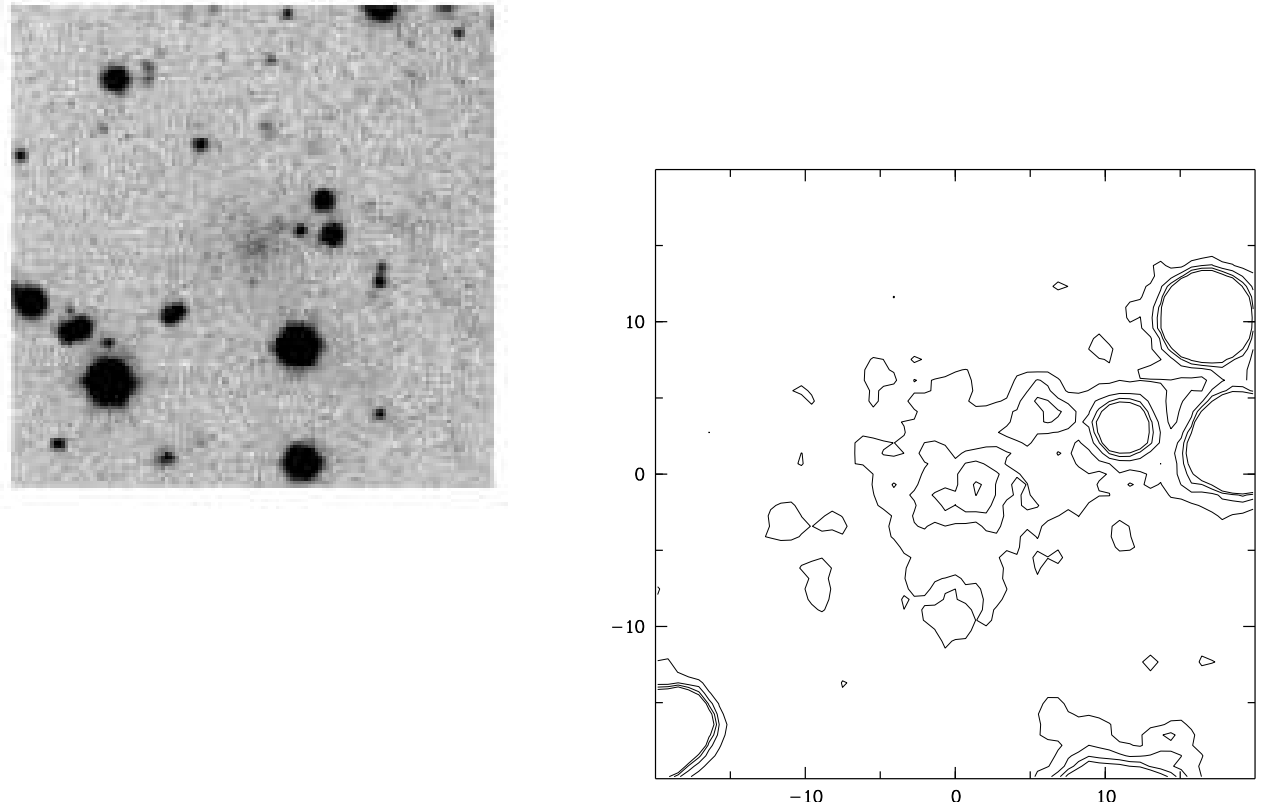


Fig. 12. AFGL 3116. *Left:* OHP 1.20 m image in the B-band. Field size: $117'' \times 117''$. *Right:* Close-up isophotes of the B-band image. Field size: $40'' \times 40''$.

τ is the optical depth along the line of sight (see Mattila 1970). For a circumstellar envelope with a constant mass loss rate, the optical depth at offset x is proportional to $x^{-1} \arccos(x/R)$ where R is the outer radius. Such a model gives a reasonable description of the well-observed profile of IRC+10216, and the fit to IRC+10011 is shown in Fig. 2. There is a degeneracy in fitting the external radius which affects the outer parts of the profile. The case shown is for $R = 50''$; if the envelope extended to a much larger radius there would be an extended x^{-1} tail in the profile with a value at $50''$ of ~ 1.2 ADU in V and ~ 1.7 ADU in B. These values are relatively small, but above the variation in the background.

The overall fits to the intensity profiles of IRC+10011 are seen to be quite good, and can be used to constrain large variations in the mass loss rate. For example, Kemper et al. (2003) have proposed that the mass loss rate of IRC+10011 may increase by a factor of 20 in the range of $\sim 3\text{--}9''$, based on modeling the intensities of CO spectra. Such a large variation would produce significant effects in the scattered light profile (in regions where $\tau \lesssim 1$). The observations show no clear deviations from constant mass loss rate, so this proposal can probably be ruled out, although this needs to be checked with the development of more complete scattering models. There may be inhomogeneities in the envelope on small size scales, perhaps

associated with the possible narrow ring structure noted in §4.3.1, which might account for the CO observations.

The profiles of the other sources are all qualitatively similar to those of IRC+10011, although OH 348.2–19.7 may have a steeper fall-off in the outer regions. In no case is there evidence for sudden, large changes in the mass loss rate on time scales longer than that of the episodic multiple arcs ($\lesssim 1000$ yr).

5.3. Envelope morphology and shaping

There are five AGB envelopes in Table 4 for which the structure is well determined by the scattered light observations on both large and small size scales. It is remarkable that only one of the five (OH 348.2–19.7) is approximately spherical throughout. Two (IRC+10216 and IRC+10011) show roughly spherical extended envelopes, and asymmetry or bipolarity close to the star; one (AFGL 2514) shows an extended, elliptical envelope; and one (AFGL 3068) shows a spiral pattern.

This sample of AGB envelopes is smaller than the sample in the CO atlas of Neri et al. (1998) (see §1) but the observations provide a sharper picture of the morphology of the envelopes. The fact that nearly all show deviations from spherical symmetry develops the scenario already implied by the case of the archetype IRC+10216 (Mauron & Huggins 2000; Skinner et al. 1998) that envelope shaping

begins on the AGB, before the transition to the proto-PN phase.

In addition to the frequent occurrence of asymmetry shown by the scattered light observations, a second striking feature is the diversity in the morphology of the envelopes. These show distinct characteristics that can be used to help identify and constrain possible shaping mechanisms.

5.3.1. Core bipolarity

There are two cases of spherical envelopes with core bipolarity, IRC+10216 and IRC+10011, as well as CIT 6 whose core is bipolar. The bipolarity is due to evacuated regions along the polar axes, and these objects are likely precursors of proto-PNe and PNe with jets, which have a similar geometry. The jets are usually ascribed to launching from the accretion disk of a binary companion that is fed by the mass loss from the AGB star (e.g., Frank & Blackman 2004). According to Garcia-Segura et al. (2005, and references therein) jets may also be launched by the AGB star, but it has been argued by Soker (2005, and references therein) that a binary companion is still needed in this situation in order to spin-up the primary.

In the cases reported here, the extent of the bipolarity is small, and the time scale is short (Table 4), much less than that of the extended envelope. In proto-PNe and young PNe, the jets are more extended. In the AGB stars the jets may be intrinsically weak, or they may have just recently turned on at full power, and may be trapped in the AGB envelope. A model for a trapped jet has been proposed for IRC+10011 by Vinković et al. (2004). Our observations show that (within the limitations of our small sample) core bipolarity is relatively common in the late AGB phase and has a very short time scale. It seems unlikely that the three cases observed here have just turned on at full power. It is more probable that the jets are weak and/or intermittent on the AGB, and gain in power or stability as the stars evolve into the proto-PNe phase.

5.3.2. Elliptical envelopes

The extended elliptical envelope found in AFGL 2514 probably has a three dimensional geometry that approximates a flattened (oblate) ellipsoid or disk, with the axis of symmetry seen in projection as the minor axis on the sky. The observed major/minor axis ratio of ~ 1.4 then implies that the diameter/thickness ratio of the ellipsoid is $\gtrsim 1.4$, with the minimum value if the system is seen edge-on, and larger values if the symmetry axis is inclined to the plane of the sky. The corresponding density contrast between the equator and the pole (at the same radius) is $q \gtrsim 2$.

It is possible that single stars undergo asymmetrical mass loss and produce elliptical envelopes (e.g., Dorfi & Hofner 1996), but the interactions of the components of a binary system lead more naturally to strong, asymmet-

Table 4. Envelope morphology in light

Star	Env. ^a	θ_{env} ($''$)	τ_{env} (yr)	Core ^a	τ_c (yr)
IRC+10216	C s	200	8700	Bp	50
IRC+10011	C s?	40	6800	Bp	75
CIT 6	? s?	25 ^b	3200 ^b	Bp	40
AFGL 2155	?	18	5700	...	
OH 348.2–19.7	C	28	12900	C	
AFGL 2514	E	40	7700	E	
AFGL 3068	Sp	42	15200	Sp	
AFGL 3099	?	20	12200	...	
AFGL 3116	?	18	5600	...	

^a Morphology: C = circular, s = shells, E = elliptical, Sp = spiral, Bp = bipolar. ^b Based on CO.

rical mass loss with a preferred plane. There are several ways in which the envelope in a binary system can acquire a flattened morphology. One example is passage through a common envelope phase. This may lead to the efficient ejection of the AGB envelope, and in the simulations by Sandquist et al. (1998) flattened systems emerge with density contrasts of $q \sim 5$. The common envelope ejection is, however, a very rapid process, and this is contrary to our observed scattered light profiles of AFGL 2514 (Fig. 6) which show a smooth, asymmetric mass loss over a long time scale. So this process can be ruled out.

A second example of a binary shaping mechanism is the gravitational focusing of the AGB wind by the companion. Simulations of this have been reported by Gawryszczak et al. (2002) and Mastrodemos & Morris (1999). For a given primary mass and wind velocity, the focusing depends on the mass and separation of the secondary. As a specific example, model 11 of Mastrodemos & Morris, which has a primary of mass $1.5 M_{\odot}$ and a secondary of mass $1.0 M_{\odot}$ with a separation of 12.6 AU, produces a density contrast $q = 2$, close to the minimum observed for AFGL 2514. A larger value of q , or a similar value of q with a smaller mass secondary, can be produced in a closer binary system.

A possible alternative mechanism is the shaping of the AGB mass loss by a stellar magnetic field. Matt et al. (2000) have shown that a stellar dipole field can focus an initially isotropic wind toward the equatorial plane, and they achieve a density contrast $q > 2$ for a plasma β parameter (the ratio of the gas to the magnetic pressure) $\lesssim 1$. For mass loss rates of $10^{-5} M_{\odot} \text{ yr}^{-1}$ this corresponds to field strengths at the stellar surface of a few Gauss. Although this type of model is plausible, Soker (2005) has pointed out that in cases where the magnetic field plays a global role in the shaping, a binary companion is necessary to maintain the field: so in this situation other binary effects (such as those discussed above) also need to be taken into account.

5.3.3. Spiral envelopes

The spiral pattern in AFGL 3068 (§4.6) shows specific characteristics that place tight constraints on a possible interpretation. First, the spiral is one-armed. Second, the pattern follows the geometry of an Archimedes spiral, with an approximately constant spacing between the arms. Third, the spiral is not planar, but is composed of thin shells, as demonstrated by the intensity profiles.

These characteristics correspond closely to the spiral shocks found in models of mass loss in binary systems investigated by Mastrodemos & Morris (1999). In this model, the mass-losing AGB star undergoes reflex motion in the binary, which results in a three-dimensional shock wave which propagates out through the envelope and creates the spiral pattern. The pitch of the spiral directly reflects the period of the binary and the shape is nearly spherical in the equatorial plane so that the observed limb-brightened spiral is little affected by moderate inclinations to the line of sight.

The radial pitch (λ) of the spiral that is given by the fit to the data in §4.6 is $2''.29$, which corresponds to 3.7×10^{16} cm at the distance of AFGL 3068. For a velocity close to the expansion velocity of the envelope (V_{exp} in Table 1), which is likely to be the case far from the star where the structure is frozen into the wind, the period is given directly by $P = \lambda/V_{exp} = 830$ yr. Using Kepler's Law, the separation of the system a is given by $a = 120(\frac{M+m}{2.5})^{1/3}$ AU, where M and m are the masses (in solar units) of the primary and secondary, respectively, and the default is for $M = 2 M_{\odot}$ and $m = 0.5 M_{\odot}$.

This period and separation are larger than the spiral shock models constructed by Mastrodemos & Morris (1999), for which the maximum separation is ~ 50 AU, but they found no evidence that the effect would not extend to wider systems. Overall, the evidence for interpreting the spiral as the interaction of a wide binary is compelling.

5.4. Binaries and PN formation

The results described above are of direct interest in connection with the possible role of binaries in the formation of PNe, which is currently an area of on-going debate (e.g., Meixner et al. 2004). One line of evidence for the importance of binaries in PN formation is the (possibly) large proportion of PN central stars with binary companions (e.g., de Marco et al. 2004). A second line of evidence is the range of morphologies of PNe which can be explained by the direct or indirect results of binary interactions, and this has been explored using population synthesis by Soker & Rappaport (2000).

Given the nature of binary interactions, an important aspect of a PN-binary scenario is that some of the effects of the interactions should be present in the precursor phases. In this context, our observations are in accord with a binary picture because most of the well observed AGB envelopes reported here show asymmetries, which are all

consistent with direct or indirect binary interactions, as discussed in the previous sections.

The diversity of the envelope morphologies reported here is also strikingly in accord with the binary scenario because the interactions depend in detail on the mass and separation of the companions. We expect that the different morphologies of the AGB envelopes reported here will lead to different morphological types of fully formed PNe. The mapping is probably not simple, and the size of our sample needs to be significantly expanded before we can investigate the statistical aspects of this in detail.

6. Conclusions

The observations reported here demonstrate that unique information on the mass-loss of AGB stars can be obtained by imaging the circumstellar envelopes in dust-scattered galactic light. The envelopes can be detected out to large distances (~ 1 kpc), and the observations provide information on the mass loss history of the stars over long time scales ($\sim 10,000$ yr).

The sample of AGB stars reported here is striking in revealing asymmetries in four out of five cases where the envelope geometry can be clearly determined. There is a diversity of morphology including a flattened system, spiral structure, and asymmetry close to the center. In all cases the asymmetries are consistent with the direct or indirect effects of a binary companion.

Our results are in accord with a binary scenario for the shaping of PNe, and further observations should lead to the possibility of classifying in detail the early shaping of the envelopes of these PN precursors.

Acknowledgements. We acknowledge the use of the MIDAS software from ESO which was used for the data processing. We thank an anonymous referee for the comments that helped improve the final version. The HST data were obtained from the ESA/ESO ST-ECF Archive Center at Garching, Germany. This work was supported in part by NSF grant AST 03-07277 (to PJH).

Appendix A: AFGL 3068

In order to demonstrate the spiral pattern in AFGL 3068 we show in Fig. A.1 the image of Fig. 8, mapped into the position angle–radius plane. The sector from -90° to 0° is repeated in the figure at 270° to 360° so that the continuity in position angle can be traced. The center of the image is determined to an accuracy of $\sim \pm 0''.15$ from the position of the star seen a longer wavelengths.

The signature of the single-armed spiral is the continuous tilted feature in the image, which can be traced around 3–4 turns, exiting from the top section of the figure and continuing from the bottom section. There is substructure in the feature, part of which is contributed by the asymmetrical illumination of the envelope.

If the bright star in Fig. 7 illuminates the envelope, it can in principle provide an independent distance to AFGL 3068. There is, however, no parallax for the star,

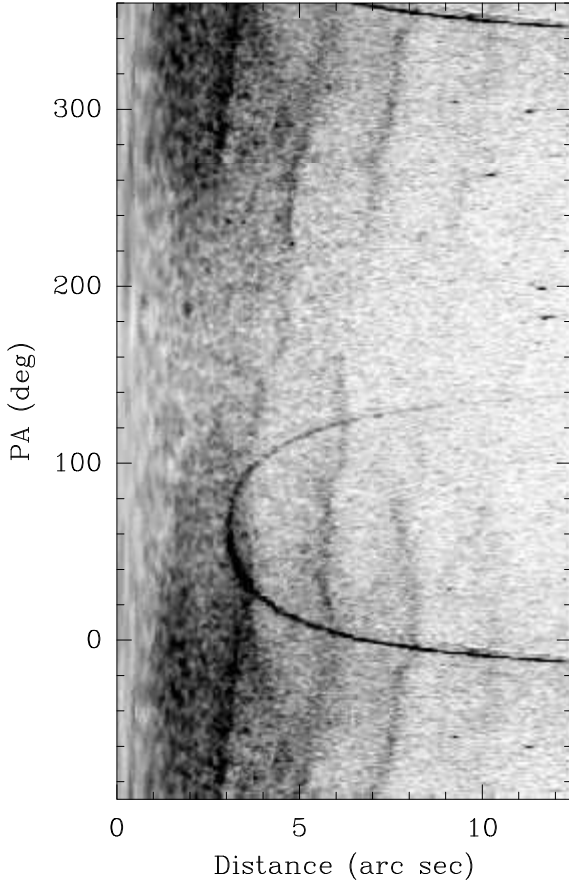


Fig. A.1. Image of AFGL 3068 of Fig. 8 mapped into the position angle-radius plane. The sector -90° to 0° is repeated at 270° to 360° to show the continuity in position angle. The curved line is the diffraction pattern of the bright star just outside the image.

and unfortunately no spectroscopic classification. Based on APM and 2MASS photometry, we find that the best color matches to stars with known spectral classifications give a spectral type of G5III or K1V. Using the absolute magnitudes given by Cox et al. (2000), the corresponding distance estimates to the star are 1800 ± 170 pc for G5III, and 155 ± 15 pc for K1V. If the star is a giant, it could illuminate the envelope, and the inferred distance would be 66% larger than the period-luminosity distance given in Table 1. If the star is a dwarf, its illumination of the envelope is ruled out. A spectroscopic classification would help clarify the issue.

References

Balick, F., & Frank, A. 2002, *ARA&A* 40, 439

Cox, A. N. 2000, *Allen's Astrophysical Quantities*, 4th edition, ed. A. N. Cox, AIP Press & Springer

de Marco, O., Bond, H. E., Harmer, D., & Fleming, A. J. 2004, *ApJ*, 602, L93

Dorf, E. A., & Höfner, S. 1996, *A&A*, 313, 605

Frank, A., & Blackman, E.G. 2004, *ApJ*, 614, 737

Garcia-Segura, G., López, J. A., & Franco, J. 2005, *ApJ*, 618, 919

Gawryszczak, A. J., Mikolajewska, K., & Różyczka, M. 2002, *A&A*, 385, 205

Hofmann, K.-H., Balega, Y., Blöcker, T., & Weigelt, G. 2001, *A&A*, 379, 529

Huggins, P. J., Olofsson, H., & Johansson, L. E. B. 1988, *ApJ*, 332, 1009

Irwin, M.J. 2000, The APM Catalog (the Web page is <http://www.ast.cam.ac.uk/~apmcat/>)

Kemper, F., Stark, R., Justanont, K., et al. 2003, *A&A*, 407, 609

Lindqvist, M., Schöier, F. L., Lucas, R., & Olofsson, H. 2000, *A&A*, 361, 1036

Lopez, J. A. 2003, in *Planetary Nebulae: their Evolution and Role in the Universe*, IAU symposium 209, ed. S. Kwok, M. Dopita, & R. Sutherland, p. 483

Loup, C., Forveille, T., Omont, A., & Paul, J. P. 1993, *A&AS* 99, 291

Martin, P.G., & Rogers, C. 1987, *ApJ*, 322, 374

Mastrodemos, N., & Morris, M. 1999, *ApJ*, 523, 357

Matt, S., Balick, B., Winglee, R., & Goodson, A. 2000, *ApJ*, 545, 965

Mattila, K. 1970, *A&A*, 9, 53

Mauron, N., & Le Borgne, J. F. 1986, *A&A*, 168, 217

Mauron, N., & Huggins, P. J. 1999, *A&A* 349, 203

Mauron, N., & Huggins, P. J. 2000, *A&A* 359, 707

Mauron, N., de Laverny, P., & Lopez, B. 2003, *AA* 401, 985

Meixner, M., Kastner, J.H., Balick, B., & Soker, N. 2004, *Asymmetrical Planetary Nebulae III: Winds, Structure, and the Thunderbird*, ASP Conf. Proceedings 313

Monnier, J. D., Tuthill, P. G., & Danchi, W. C. 2000, *ApJ*, 545, 947

Monnier, J. D., Millan-Gabet, R., Tuthill, P. G., et al. 2004, *ApJ*, 605, 436

Neri, R., Kahane, C., Lucas, R., et al. 1998, *AA Suppl.* 130, 1

Olivier, E. A., Whitelock, P., & Marang, F. 2001, *MNRAS*, 326, 490

Sandquist, E., Taam, R. E., Lin, D.N.C., & Burkert, A. 1998, *ApJ*, 506, L65

Schmidt, G. D., Hines, D. C., & Swift, S. 2002, *ApJ*, 576, 429

Skinner, C. J., Meixner, M., & Bobrowsky, M. 1998, *MNRAS* 300, L29

Soker, N. 2005, in *Planetary Nebulae as Astronomical Tools*, ed. R. Szczerba, G. Stazinska, S. K. Gorny, American Institute of Physics Conference Proceedings, vol. 804, 89

Soker, N., & Rappaport, S. 2000, *ApJ*, 538, 241

Trammell, S. 1999, in *International Symposium on Astrophysics Research and Science Education*, ed. C. D. Impey, Vatican Observatory, 200

Vinković, D., Blöcker, T., Hofmann, K.-H., Elitzur, M., & Weigelt, G. 2004, *MNRAS*, 352, 852

Weigelt, G., Balega, Y. Y., Blocker, T., et al. 2002, *A&A*, 392, 131

Online Material

List of Objects

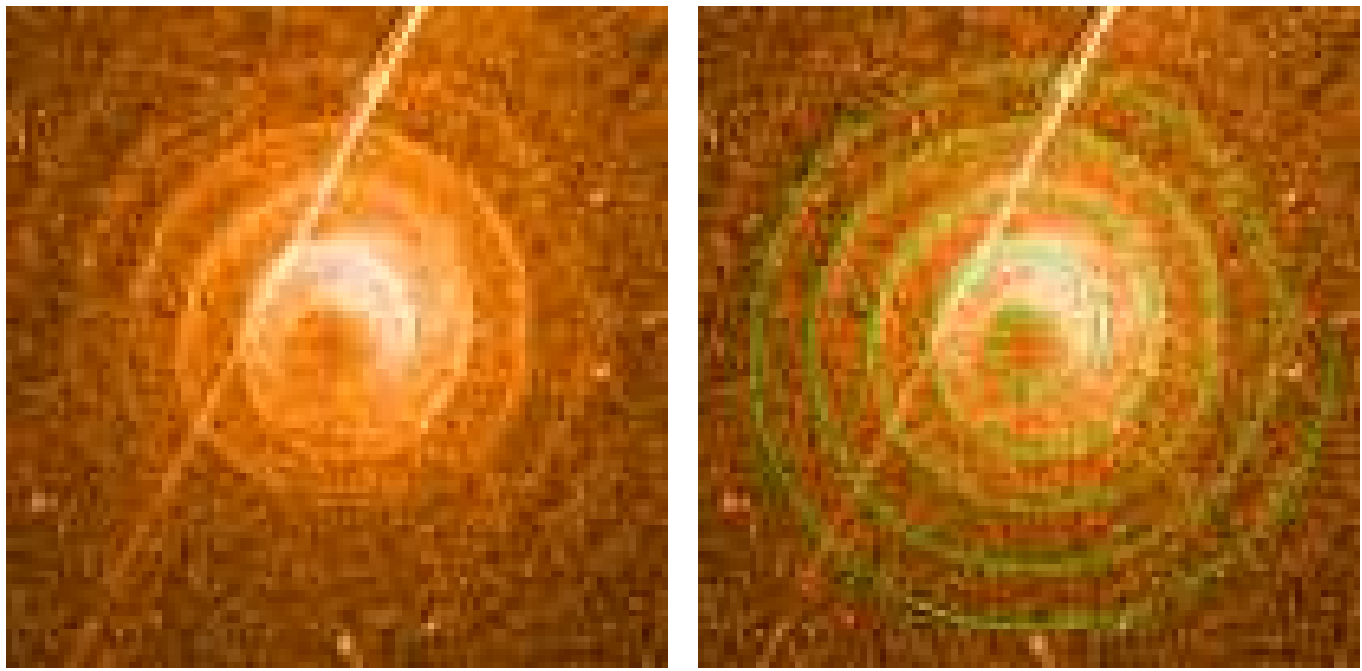


Fig. A.2. AFGL 3068. *Left:* Close-up of HST-ACS image in the F606W filter, lightly smoothed with a Gaussian of width (FWHM) 1.5 pixels. Field size: $25.\overset{\prime}{6} \times 25.\overset{\prime}{6}$. *Right:* Same image, with Archimedes spiral fit. See text for details.

- ‘AFGL 3068’ on page 12
- ‘IRC+10216’ on page 12
- ‘IRC+10216’ on page 13
- ‘IRC+10011’ on page 13
- ‘IRC+10011’ on page 13
- ‘AFGL 2514’ on page 13
- ‘IRC+10216’ on page 13
- ‘IRC+10011’ on page 13
- ‘CIT 6’ on page 13
- ‘AFGL 2155’ on page 13
- ‘OH 348.2–19.7’ on page 13
- ‘AFGL 2514’ on page 13
- ‘AFGL 3068’ on page 13
- ‘AFGL 3099’ on page 13
- ‘AFGL 3116’ on page 13
- ‘AFGL 2514’ on page 13
- ‘AFGL 2514’ on page 13
- ‘AFGL 3068’ on page 14
- ‘AFGL 3068’ on page 15
- ‘AFGL 3068’ on page 3